EMC3-EIRENE Simulation of the Magnetic Field Ripple Effect on Edge Impurity Flows in Heliotron J

F. Cai[1], S. Kado[2], G. Kawamura[3,4], R. Matoike[5], S. Ohshima[2], T. Minami[2], S. Inagaki[2], F. Kin[2], S. Kobayashi[2], A. Ishizawa[1], Y. Nakamura[1], H. Okada[2], S. Konoshima[2], T. Mizuuchi[2], Y. Feng[6], H. Frerichs[7], K. Nagasaki[2]

[1] *Graduate School of Energy Science, Kyoto University, Uji, Japan*
[2] *Institute of Advanced Energy, Kyoto University, Uji, Japan*
[3] *National Institute for Fusion Science, National Institutes of Natural Sciences, Toki, Japan*
[4] *The Graduate University for Advanced Studies, SOKENDAI, Toki, Japan*
[5] *National Institutes for Quantum Science and Technology, Naka, Japan*
[6] *Max-Planck Institute for Plasma Physics, Greifswald, Germany*
[7] *University of Wisconsin-Madison, Wisconsin, U.S.A.*

1. Introduction

Impurity transport in the edge region in the magnetically confined fusion-relevant plasma is an important topic in sustaining a high-performance plasma. Helical ripple in magnetic field is a common feature among helical devices. Finding the response of impurity on ripple structure helps to understand and control the impurity behavior in the edge region of helical devices.

In this study, we found that plasma and impurity parameters have a response to the ripple structure in Heliotron J, based on EMC3-EIRENE simulation [1]. Concentration and reduction of impurity density at ripple peaks were observed and was explained from the transport analysis on force balance along a magnetic field line.

2. Helical ripple in edge plasma

Heliotron J is a helical axis heliotron device with pole number $l = 1$, major radius $R \approx 1.2$ m and a toroidal period number of $N = 4$. Natural islands are created on the resonant surface which work as a divertor to separate a confined region from the plasma facing component. Region around the natural islands is known as scrape-off layer (SOL). Natural islands wind around the confined region helically, Fig. 1. In the standard configuration [2], the toroidal to poloidal field ratio of natural islands is $n/m = 4/7$. The distance in toroidal angle in which a field line in SOL undergoes a single poloidal rotation is $\Delta\phi = 2\pi m/n = 630°$. The number of times the field line encounters the position of helical coil during the travel towards the toroidal direction every $\Delta\phi$ is $N_{\mathrm{rip}} = l|1 - N\Delta\phi/2\pi| = 6$. The parallel scale length of the ripple structure, $L_B = B/\nabla_{\parallel}B$, can be estimated by $L_B \sim R\Delta\phi/2N_{\mathrm{rip}} \approx 1$ m.

Magnetic field strength on a divertor leg is plotted in Fig. 2 in a simplified coordinate system. The horizontal axis is one of four toroidal symmetric period $\Delta\phi$. Vertical axis is an approximate radial distance from the X-point. Objects painted in white indicate the target plates

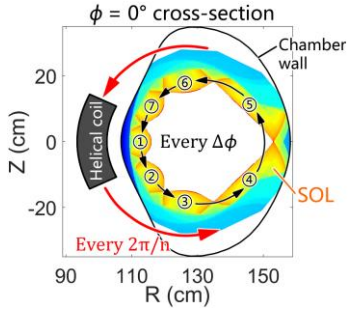

Fig. 1. Helical rotation of natural islands and helical coil in Heliotron J.

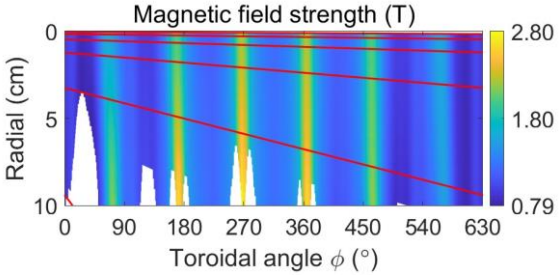

Fig. 2. Distribution of magnetic field strength on a divertor leg.

or the chamber wall. In Heliotron J, chamber wall directly works as target plates. Red lines are the field lines tangent to target plates. Field lines travel from left to right and up to down in sequence in each layer divided by the red lines.

The ripples in magnetic field strength distribution along a field line are created when a field line approaches and moves away from a helical coil, because field strength on a field line is inversely proportional to the distance to coil approximately. In each toroidal period, a field line encounter $N_{\mathrm{rip}} = 6$ ripple peaks.

3. Nozzle effect

In the downstream region of SOL, the parallel and perpendicular components of fluid velocity usually satisfy $u_{\parallel \mathrm{i}}/u_{\perp \mathrm{i}} \gg L_B/L_\perp$, where $L_\perp \approx 5$ cm is the thickness of SOL. Hence, plasma can be considered to be frozen in the field line under the scale of the ripple structure. Terms including $u_\perp$ can be neglected in the moment equations. Then the plasma continuity and parallel-momentum conservation equations are reduced to Eq. (1) and (2) respectively.

$$\boldsymbol{\nabla} \cdot \left(\frac{n_{\mathrm{i}} u_{\parallel \mathrm{i}}}{B} \boldsymbol{B} \right) = 0 \quad (1) \qquad \boldsymbol{\nabla} \cdot \left(\frac{m_{\mathrm{i}} n_{\mathrm{i}} u_{\parallel \mathrm{i}}^2}{B} \boldsymbol{B} \right) = -\nabla_\parallel p \quad (2) \qquad \nabla_\parallel T_{\mathrm{e,i}} = 0 \quad (3)$$

Here we assumed steady state, quasi-neutral, current-free, inviscid and source-free conditions. n_{i} is the ion density. $\boldsymbol{B}$ is the magnetic field vector. $B = |\boldsymbol{B}|$ is the magnetic field strength. m_{i} is the mass of plasma ion. $p = n_{\mathrm{i}}(T_{\mathrm{i}} + T_{\mathrm{e}})$ is plasma total pressure. $\nabla_\parallel \equiv B^{-1}\boldsymbol{B} \cdot \boldsymbol{\nabla}$ is parallel spatial derivative operator.

Due to the large parallel heat conductivity in SOL, the parallel scale length of electron and ion temperature usually are negligible compared with ripple scale, i.e., $\nabla_\parallel T_{\mathrm{e,i}} \ll T_{\mathrm{e,i}}/L_B$, Fig. 4(c)(d). Thus, it is acceptable to assume an isothermal condition when considering the ripple effect to have Eq. (3). Considering $\boldsymbol{\nabla} \cdot \boldsymbol{B} = 0$, the solution of Eq. (1), (2) and (3) is given by Eq. (4) and (5).

$$\frac{n_{\mathrm{i}}}{n_{\mathrm{i}}^*} = \exp\left(\frac{1 - M^2}{2}\right) \quad (4) \qquad \frac{B}{B^*} = M \exp\left(\frac{1 - M^2}{2}\right) \quad (5)$$

where $M = u_{\parallel \mathrm{i}}/C_{\mathrm{s}}$ is the parallel Mach number, $C_{\mathrm{s}} = m_{\mathrm{i}}^{-1/2}(\partial p/\,\partial n_{\mathrm{i}})^{1/2} = (p/m_{\mathrm{i}}n_{\mathrm{i}})^{1/2}$ is ion sound speed under isothermal condition. n_{i}^* and B^* are the corresponding value of ion density and field strength at $M = 1$. The same conclusion is also derived in [3].

The dependence in Eq. (5) is plotted in Fig. 3. The behavior of plasma fluid in the magnetic field ripple in SOL can be treated as in an isothermal nozzle with flux tube cross-section area inversely proportional to B. In fact, if we replace the isothermal condition (3) with the adiabatic condition, a similar relation between Mach number and magnetic field strength as in a widely known adiabatic nozzle can be derived, Fig. 3. There are two regimes in a nozzle:

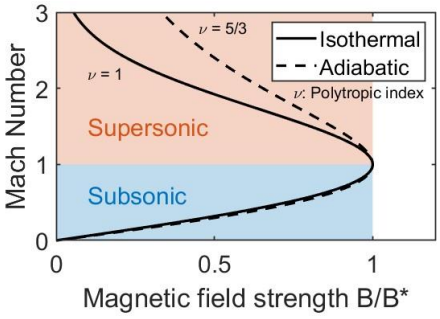

Figure 3. Regimes in nozzle.

1) *Subsonic regime* ($0 < M < 1$): $\mathrm{d}M/\mathrm{d}B > 0$ and $\mathrm{d}n_{\mathrm{i}}/\mathrm{d}B < 0$.

2) *Supersonic regime* ($M > 1$): $\mathrm{d}M/\mathrm{d}B < 0$ and $\mathrm{d}n_{\mathrm{i}}/\mathrm{d}B > 0$.

For a given magnetic field strength, whether the solution in Eq. (4) and (5) is subsonic or supersonic is determined by upstream or downstream condition of the nozzle.

Transport of plasma and impurity in the edge region of Heliotron J is simulated by 3D Monte Carlo code EMC3-EIRENE. The plasma ion is deuterium. Impurity carbon is generated by sputtering on the target plate with a sputtering yield of $Y = 0.01$. Cross-field diffusion coefficients of plasma and impurity are $D = 0.5\ \mathrm{m}^2 \cdot \mathrm{s}^{-1}$ and $D_{\mathrm{imp}} = 1\ \mathrm{m}^2 \cdot \mathrm{s}^{-1}$. Electron and

ion cross-field heat conductivities are $\chi_e = \chi_i = 2\,m^2 \cdot s^{-1}$. Heating power is $P_{SOL} = 200$ kW. No external particle and impurity source. Two conditions are simulated, with low ($1.2 \times 10^{19}\,m^{-3}$) or high ($6.0 \times 10^{19}\,m^{-3}$) electron density on the inner boundary. The distribution of plasma parameters on a divertor leg, similar with Fig. 2, under the low-density condition are plotted in Fig. 4. EMC3-EIRENE is not capable to treat supersonic flow, limited by its algorithm in the STREAMING module [4]. Plasma parameters response to the magnetic ripple as in the subsonic regime of an isothermal nozzle that Mach number is increased, while electron density is reduced, in the ripple peaks. The simulation under the high-density condition gives the same response. The same phenomenon is also observed in the simulation on LHD [5].

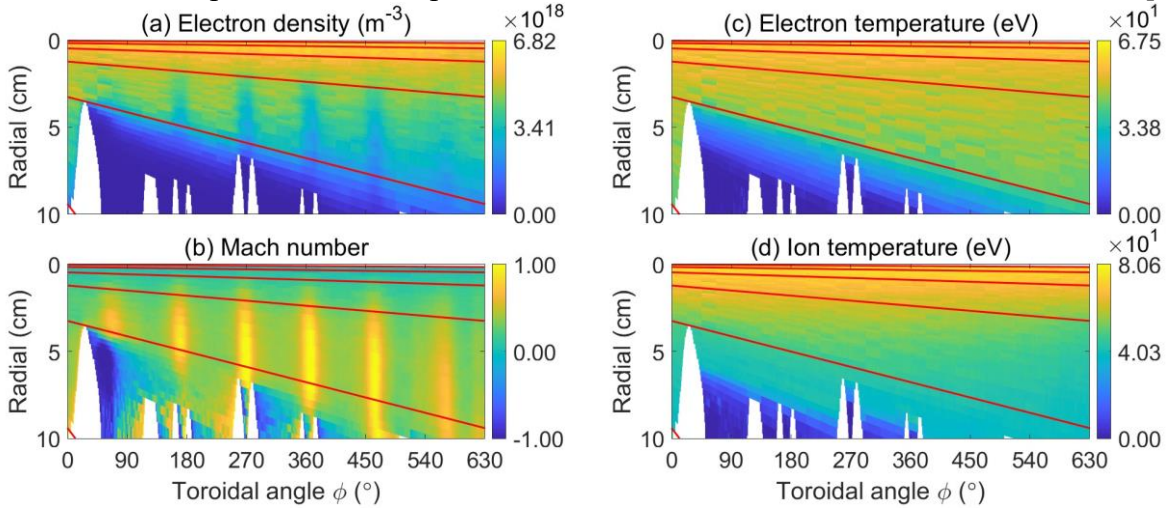

Fig. 4. Distribution of (a) electron density, (b) Mach number, (c) electron temperature, (d) ion temperature, on a divertor leg under low-density condition.

4. Impurity response

Concentration and reduction of impurity density is found in the ripple peaks under low- and high-density conditions respectively, Fig. 5. Densities of some of the charge ions are not shown is this article due to the weak response or large Monte Carlo noise under certain conditions. The following interpretation is based on the fluid model for impurity transport in EMC3 [6]. Impurity continuity and parallel-momentum conservation are given by Eq. (6) and (7) respectively.

$$\nabla \cdot \left(\frac{n_Z u_{\parallel Z}}{B}\boldsymbol{B}\right) = 0 \qquad (6) \qquad\qquad \nu_{Zi} m_I n_Z (u_{\parallel Z} - u_{\parallel i}) = -T_i \nabla_\parallel n_Z + Z n_Z e E_\parallel \qquad (7)$$

where $\nu_{Zi} \propto n_i T_i^{-3/2}$ is the collision frequency. n_Z and $u_{\parallel Z}$ are the density and parallel fluid velocity of Z-charged impurity. m_I is the mass of the impurity ion. The three terms in Eq. (7) are friction force, pressure gradient and electric field force respectively. Already considered Eq. (3) and $T_Z = T_i$ is defined in EMC3. Also, magnetic freezing and source free for impurity ions were assumed like Eq. (1). Parallel electric field is given by generalized Ohm's law: $T_e \nabla_\parallel n_e + n_e e E_\parallel = 0$, results in $n_e \propto \exp(e\varphi/T_e)$. Due to the nozzle effect, ion density is reduced in ripple peaks, so electric potential dips are created to drag electron away from the ripple peaks to maintain quasi-neutrality, Fig. 6(c)(f). Consider two extreme regimes:

1) *Weak collisional regime*: with low n_i and large T_i that ν_{Zi} tends to zero. The friction force is negligible, so Eq. (7) gives $n_Z \propto \exp(-Ze\varphi/T_i)$. Due to the potential dip created by nozzle, impurity has a concentration in the ripple peaks. Since $dn_Z/d\varphi \propto -Z$, The higher the charged number the sharper the density peaks are, Fig. 6(a). Besides, perpendicular transport is enhanced by large perpendicular density gradient in ripple peaks. Impurity particle fluxes are towards ripple peaks to supply the perpendicular diffusional loss, hence impurity fluid

velocities tend to be positive at the upstream of each ripples while be negative at the downstream, Fig. 6(b).

2) *Collisional regime*: with large n_i and low T_i that ν_{Zi} tends to infinite. Right-hand side of Eq. (7) is negligible, results in $u_{\|Z} = u_{\|\mathrm{i}}$, that impurity is frozen with plasma, Fig. 6(e). Considering Eq. (6) is the same as (1), there should be $n_z \propto n_\mathrm{e}$ to have the impurity density reduction in the ripple peaks, Fig. 6(d).

Based on the analysis above, the response of impurity to the ripple structure is explained.

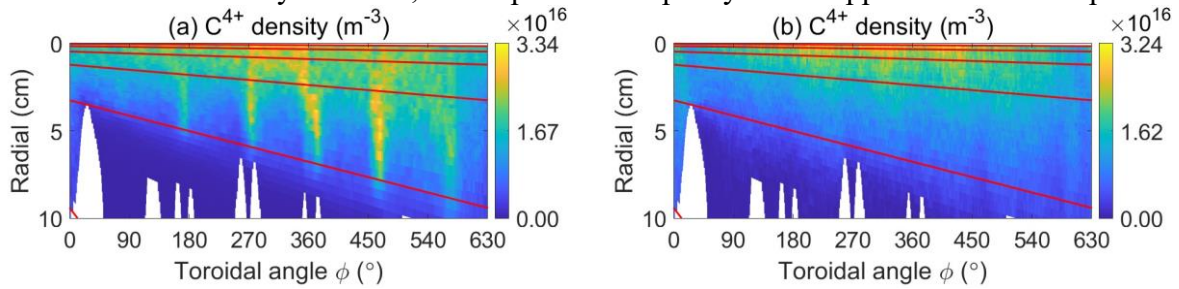

Fig. 5. Distribution of C^{4+} densities on a divertor leg under (a) low-density condition, (b) high-density condition.

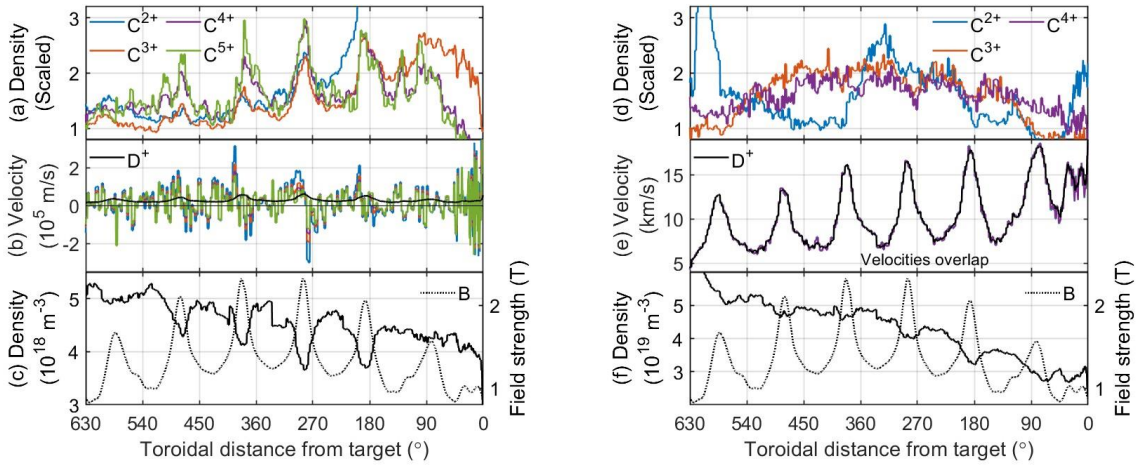

Fig. 6. Distribution of densities, fluid velocities and magnetic field strength along a field line, (a)(b)(c) under low-density condition, (d)(e)(f) under high-density condition.

5. Summary

Helical magnetic ripple is found in the edge region of Heliotron J, which works as an isothermal nozzle for plasma based on fluid description. Plasma is accelerated with an ion density dip in the ripple peaks, resulting in an electric potential dip. Impurity density has a concentration or reduction under low- or high-density condition respectively.

Acknowledgements

This work was supported by JSPS Core-to-Core Program, A. Advanced Research Networks, "PLADyS" and by the NIFS Collaboration Research Program (NIFS22KUHL108).

Reference

[1] R. Matoike *et al*., Plasma and Fusion Research **14** (2019) 3403127.
[2] T. Mizuuchi *et al*., J. Plasma Fusion Res. SERIES **3** (2000) 192-196.
[3] S. Togo *et al.*, Contribution to Plasma Physics **58** (2018) 559-562.
[4] Y. Feng *et al.*, Plasma Phys. Control. Fusion **64** (2022) 125012.
[5] M. Kobayashi *et al.*, Fusion Sci. Technol. **58** (2010) 220.
[6] Y. Feng *et al.*, Plasma Phys. Control. Fusion **44** (2002) 611–625.